

# Iterative Learning Control for Robotic Deposition Using Machine Vision

David J. Hoelzle, *Student Member, IEEE*, Andrew G. Alleyne, *Senior Member, IEEE*, and Amy J. Wagoner Johnson

**Abstract**—This work presents a new application of Iterative Learning Control (ILC) in two respects. Firstly, the output signal is generated by a machine vision system. Secondly, ILC is applied to the extrusion process in Micro Robotic Deposition ( $\mu$ RD), directly addressing the end product quality instead of contributors to end product quality such as position tracking. A P-type and model inversion learning function are both applied to the extrusion process, a system that has nonlinear dynamics and no readily available volumetric flowrate sensor. Theoretical and experimental results show that the nominal system is first order with a pure time delay. Both P-type and model inversion ILC improve the dynamics, with both systems providing better reference tracking. The ILC compensates for the unmodeled nonlinearities, realizing a reduction of RMS error to less than 20% of the initial value for the model inversion approach. Experiments are performed, displaying the ability to extrude precise and seamless closed shapes with the model inversion ILC. This is a necessary requirement for transitioning materials and embedding sensors in multi-material  $\mu$ RD.

## I. INTRODUCTION

ITERATIVE Learning Control (ILC) has been successfully applied to reference tracking problems on a variety of different machines used in repetitive manufacturing processes[1]. However, using ILC to control an actual process, not the positioning of manufacturing toolbits, has received less attention[2]. A potential application of ILC implemented into process control is the modulation of build material flowrate in Micro Robotic Deposition ( $\mu$ RD).  $\mu$ RD is a Solid Free-Form fabrication process in which a colloidal ink is extruded through a nozzle in a defined trajectory to build three-dimensional structures[3]. The ceramic colloidal ink of interest here has carefully tailored viscoelastic properties to facilitate ink flow through a nozzle while

This work was supported in part by NSF DMI-014066 and Nano-CEMMS Center NSF Award # 0328162.

A. G. Alleyne is with the Mechanical Science and Engineering Department at the University of Illinois at Urbana-Champaign, Urbana, IL 61801 USA (phone: 217-244-9993; fax: 217-244-6534; e-mail: alleyne@uiuc.edu).

D. J. Hoelzle is with the Mechanical Science and Engineering Department at the University of Illinois at Urbana-Champaign, Urbana, IL 61801 USA (e-mail: hoelzle2@uiuc.edu).

A. J. Wagoner Johnson is with the Mechanical Science and Engineering Department at the University of Illinois at Urbana-Champaign, Urbana, IL 61801 USA (e-mail: ajwj@uiuc.edu).

maintaining a stiffness appropriate for spanning structural gaps up to 2 mm[4]. These properties allow the fabrication of porous structures without the use of lost molds, making  $\mu$ RD a good fabrication method for applications such as artificial bone scaffolds[5,6], piezoelectric actuators[7], micro-fluidic networks[8], and photonic bandgap structures[9]. A schematic of the process and the micro-extrusion system are shown in Figure 1.

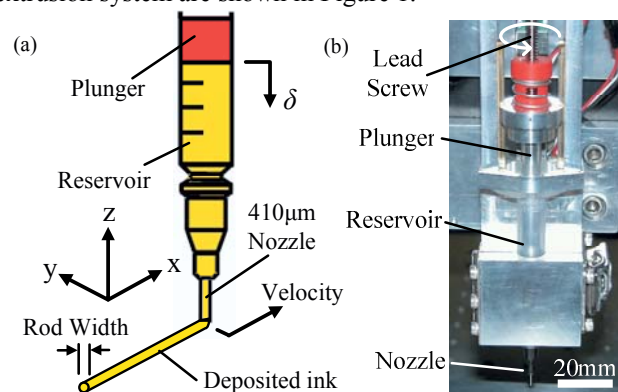


Fig. 1. Micro-extrusion system. (a) Schematic of system. Ink is extruded in the form of rods. (b) Extrusion mechanism.

Although  $\mu$ RD has been proven useful in these applications, the structural complexity for each application is limited by two factors: 1)  $\mu$ RD can only operate in steady-state, requiring lead-in lines and continuous material extrusion and 2) an appropriate material flowrate sensor has yet to be developed. With the advent of precise material flowrate modulation, the fabrication of complex structures, such as those with embedded sensors, multiple material properties, material discontinuities, and near-net shape fabrication, will be enabled. An example of an embedded sensor is shown schematically in Figure 2. Here a resistive element could span the interstices of this lattice structure to measure strain when the structure is loaded. The deposition of this sensor would require the precise starting and stopping of ink flow, hence the motivation for the pulse-type input tested in this research.

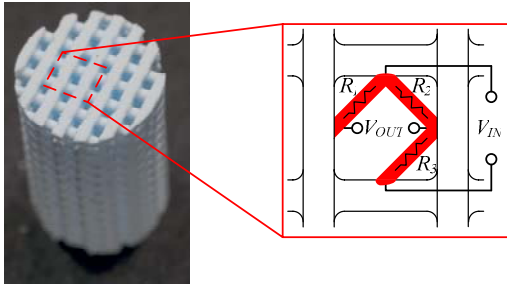


Fig. 2. Embedded resistive element to measure strain in the lattice on the left.

There are a few challenges inherent to the  $\mu$ RD process that makes ILC an appropriate control technology. As previously stated, there is currently no real-time material flowrate sensor available. Instead, the material flowrate can only be inferred after the process is complete, eliminating the use of simple PID and lead-lag type controllers for feedback control of material flowrate. For implementation in an ILC framework, the material flowrate can be calculated offline, processed by the ILC algorithm, and a new control signal can be applied to the next iteration. Another challenge is that the material flowrate has a highly nonlinear response. Feedforward techniques such as feedforward model inversion have been shown to improve material flowrate modulation[10,11], however the system nonlinearities and modeling errors ultimately limit the effectiveness of this technique. Instead, feedforward ILC has the capability to learn these nonlinearities and the correct system model, thereby providing a precise method to modulate material flowrate.

This paper proceeds as follows. The vision system implemented into the ILC framework and a validation of measurement accuracy are presented in Section II. Section III presents the development of a model of the nominal extrusion system response along with experimental validation. Section IV presents experimental results from a P-type and a model inversion ILC system and compares the results of the two control algorithms. Section V displays the use of ILC to precisely modulate the ink flowrate when depositing two closed shapes. Simple shapes such as these are applicable to embedded sensor deposition. Section VI provides conclusions and future work.

## II. VISION SYSTEM

Vision systems can be used to examine the end product or part characteristics at fabrication check points to provide sufficient information to significantly improve quality. ILC by nature is conducive to the use of vision measurement systems. Image data can be stored during fabrication, processed offline between iterations, and then used for the new control signal for the next iteration. There are a vast number of potential applications of image based ILC for manufacturing beyond  $\mu$ RD, including stamping, forming, and injection molding. Images of stamped, formed, or molded finished parts could be compared to an ideal shape

contour and used as the output signal in ILC.

Here a vision system is implemented into an ILC framework for the  $\mu$ RD process. A typical  $\mu$ RD robot[12] is modified to include a video camera and lighting system focused on the nozzle tip, Figure 3. During a deposition cycle, video of the extrusion of the white colloidal ink onto a contrasting black substrate is recorded. At each point in time, the rod width at the outlet is measured from thresholded images of the individual video frames. Volumetric flowrate is calculated from the rod width using a piecewise continuous function (1) based on an assumed geometry of the rod cross-section, Figure 4, and the deposition velocity, equation (3). The cross-section is assumed to be a circle flattened at the top and bottom by the nozzle and substrate respectively. Cross-section images, not shown[10], along with  $\mu$ RD literature[3] support this geometric assumption. Volumetric flowrate has been similarly measured in [13], but instead using a less automated technique.

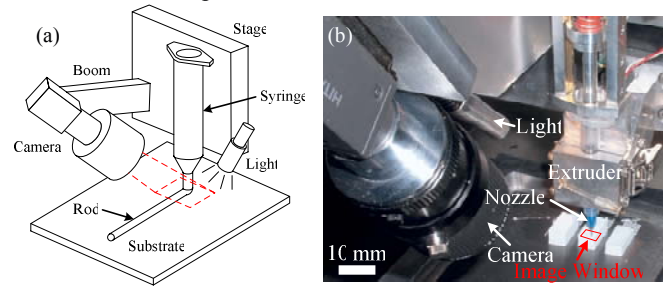


Fig. 3. Machine vision system. (a) Schematic of vision system. Camera and light move along with the deposition system to maintain a constant image window. (b) Image of vision system.

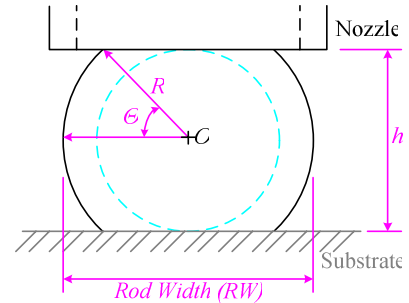


Fig. 4. Assumed rod cross-section.  $O$  is equidistant from the nozzle and substrate.

$$A_{CS} = \pi R^2; \quad \text{for } 0 \leq RW \leq h$$

$$A_{CS} = 2\theta R^2 + \frac{1}{2}h^2 \frac{1}{\tan \theta}; \quad \text{for } RW > h \quad (1)$$

where:

$$R = \frac{1}{2}RW \text{ and } \theta = \sin^{-1} \left( \frac{h/2}{R} \right) \quad (2)$$

and the flowrate is simply calculated by:

$$Q_{out} = A_{CS}v; \quad v = 5 \text{ mm/s} \quad (3)$$

There are several steps that need to be taken to develop a precise and accurate vision measurement system. Foremost, the camera and lighting must be carefully adjusted to capture

and properly illuminate the entire extruded rod so that reflections are not interpreted as the ink after thresholding images. In video based systems, the video must be segmented, the individual frames cropped to the appropriate size, and the images spliced back together to capture the entire deposition process. Here we demonstrate the accuracy of this measurement system in Figure 5. First, a finite length of wire is measured as if it was extruded ink, Figure 5a. The vision system measurement accurately calculates the rod width, as nominally measured by calipers, within 0.05 mm at the middle of the wire. Next, the segmentation, image cropping, and splicing of images is tested by measuring the width of a V-shaped printout as the video system pans over the top. If the image is properly reconstructed from video, the resultant measurement will increase linearly without discontinuities. Figure 5b displays a linear signal with slight discontinuities that are mainly attributed to pixilation of the actual printout. Furthermore, the images in Figure 14 are each 9 spliced together segments of video, showing nearly imperceptible transitions between segments. Tasks such as these will need to be addressed to accurately measure system outputs in other vision based ILC systems. Additional tasks, such as image alignment, feature recognition, correcting video unsteadiness and focal length inconsistencies, and computation time optimization can be anticipated in other applications.

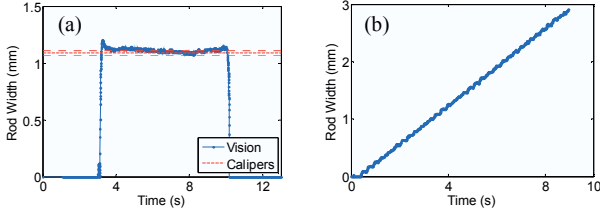


Fig. 5. Two tests of the machine vision system. (a) Accuracy test. Red lines represent mean wire width and one standard deviation from mean width. 5 caliper measurements. (b) Image consolidation test. A perfectly measured signal would be perfectly linear.

### III. MODEL DEVELOPMENT

The micro extrusion system controlled here uses a plunger to apply pressure to a reservoir of ink, which in turn extrudes ink through a nozzle in the form of cylindrical rods, Figure 1a. The plunger is driven by a motor and lead screw mechanism, Figure 1b, and the entire mechanism is mounted to a XYZ motion system. For the purpose of developing a simple model, the motion system and plunger dynamics are assumed to be sufficiently faster than the slow ink dynamics and are therefore ignored.

The ink dynamics are modeled in two parts, first considering the compressible ink in the syringe reservoir as a control volume, Figure 6a, and second as a non-Newtonian fluid flowing through a nozzle, Figure 6b. The model provides a transfer function relating the input (plunger displacement speed), and the output (volumetric flowrate at

the nozzle exit). Beginning with the control volume model in the syringe reservoir, with reasonable assumptions the compressible ink has the flow-pressure relationship in equation (4).

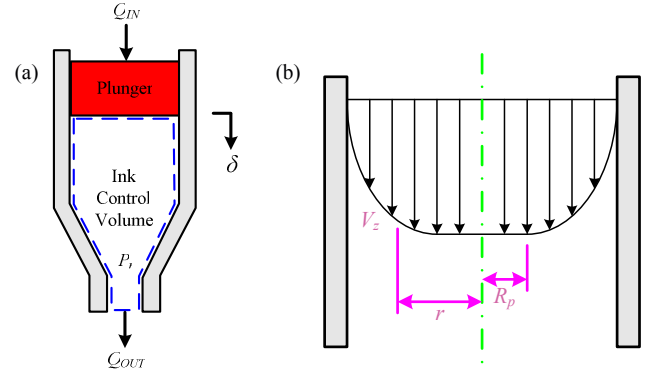


Fig. 6. Schematics for model development. (a) Control volume of ink within syringe reservoir. (b) Velocity distribution,  $V_z$ , of yield-pseudoplastic ink flowing through a nozzle. Center of nozzle is an unyielding core of ink with radius  $R_p$ , surrounded by a shear-thinning outer layer at the nozzle wall.

$$\frac{V_r}{\beta_i} \frac{dP_r}{dt} = Q_{in} - Q_{out} \quad (4)$$

where the reservoir volume and control volume inflow in (4) are a function of plunger displacement:

$$V_r = V_{r,0} - A_{CS} \delta \quad \text{and} \quad Q_{in} = A_{CS} \dot{\delta} \quad (5)$$

$V_r$  = Volume of ink in reservoir

$\beta_i$  = Ink bulk modulus

$P_r$  = Reservoir pressure

$A_{CS}$  = Cross-sectional area

$\delta$  = Plunger displacement

$Q_{in}$  = Control volume inflow

$Q_{out}$  = Control volume outflow

Next the model for ink flow through the nozzle is developed. The non-Newtonian colloidal ink is characteristic of a yield-pseudoplastic fluid. Yield-pseudoplastic fluids are extremely non-linear. They behave as a solid when unstressed and do not deform until a shear stress above their yield stress is achieved[14]. Above the yield stress the fluid is pseudoplastic, or shear-thinning, meaning that the ink becomes less viscous as the shear rate increases. Laminar flow of a yield-pseudoplastic fluid through a nozzle can be modeled by (6)[14]:

$$Q_{out} = \pi R^3 n \left( \frac{-\tau_w}{m} \right)^{1/n} (1-\phi)^{(n+1)/n} \times \left\{ \frac{(1-\phi)^2}{3n+1} + \frac{2\phi(1-\phi)}{2n+1} + \frac{\phi^2}{n+1} \right\} \quad \text{for } \phi \leq 1 \quad (6)$$

$Q_{out} = 0$  for  $\phi > 1$   
where:

$$\phi = \frac{\tau_y}{\tau_w} \quad \text{and} \quad \tau_w = \left( -\frac{P_r}{L} \right) \frac{R}{2}, \quad (7)$$

with the following parameters.

$R$  = Nozzle radius                       $L$  = Nozzle length  
 $n$  = Flow behavior index                 $m$  = Fluid consistency coefficient  
 $\tau_w$  = Nozzle wall shear stress         $\tau_y$  = Ink yield stress

$m$  and  $n$  are empirically derived parameters which describe the ink characteristics and can vary significantly between different ink materials and even between batches of ink.

The nonlinear equation in (6) is not conducive to the development of a simple model to be used in the proof of concept study here. If we assume the yield stress is small, therefore assuming the fluid to be pseudoplastic instead of yield-pseudoplastic, equation (8) replaces (6)[14]. Furthermore, some of the parameters in (8) are constant during a given experiment and can be consolidated into the simpler equation (9), where the coefficient,  $C$ , and the denominator,  $D$ , are the consolidated constants.

$$Q_{out} = \pi \left( \frac{n}{3n+1} \right) \left( \frac{P_r}{2mL} \right)^{1/n} R^{(3n+1)/n} \quad (8)$$

$$Q_{out} = C \left( \frac{P_r}{D} \right)^{1/n} \quad (9)$$

Combining equations (4) and (9) gives:

$$\frac{V_r}{\beta_i} \frac{nD}{C} \left( \frac{P_r}{D} \right)^{1-1/n} \dot{Q}_{out} + Q_{out} = A_{CS} \delta \quad (10)$$

Local linearization about some nominal reservoir volume,  $V_{r0}$ , and pressure,  $P_{r0}$ , results in a first order approximation of the ink outflow response to plunger velocity where the delay,  $\lambda$ , captures the time taken to exceed the material yield stress.

$$\frac{Q_{out}(s)}{\delta}(s) = \frac{K}{\tau s + 1} e^{-\lambda s} \quad (11)$$

The steady-state gain and time constant are:

$$K = A_{CS} \text{ and } \tau = \frac{V_{r0}}{\beta_i} \frac{nD}{C} \left( \frac{P_{r0}}{D} \right)^{1-1/n} \quad (12)$$

An experiment using the nominal reference signal (pulse-type input) as the control signal validates model (11). Figure 7 shows the mean nominal response of 10 trials. Table I presents the first order system parameters determined by fitting model (11) to the experimental data. The experimental data agrees well with the continuous time model and the discrete time version used for model inversion ILC in Section IV. The experimental data does deviate from the model at the end of the response where there are oscillations in the flowrate data. These oscillations capture the intermittent flow behavior of the ink well after the falling step of the pulse-type input, Domain D, seen in Figure 8. The intermittent flow behavior results from the compressed ink seeping out of the nozzle, attaching to the substrate, and dragging a section of the highly cohesive ink out of the nozzle until the section breaks and the process restarts. At these low flowrates, model (11) fails to account for this oscillatory behavior.

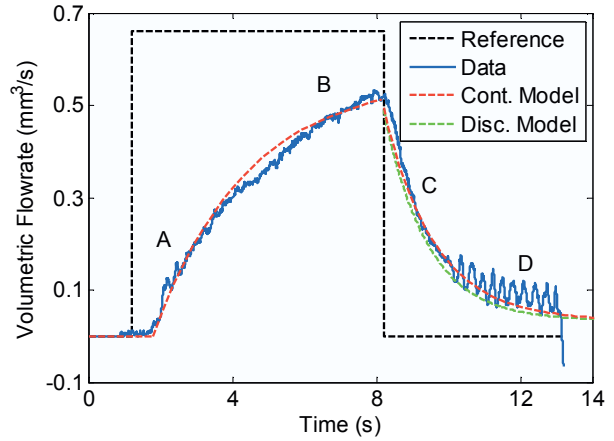


Fig. 7. Nominal response to the pulse-type input. Data is the mean of 10 trials. Response is divided into 4 domains, (A) rising step response, (B) steady-state response, (C) falling step response, (D) and intermittent flow behavior domain.

TABLE I  
NOMINAL PLANT FIRST ORDER DYNAMICS

Parameter	Rising Step (A)	Falling Step (C)
$K$	0.85	0.70
$\tau$ (s)	2.6	1.4
$\lambda$ (s)	0.6	0

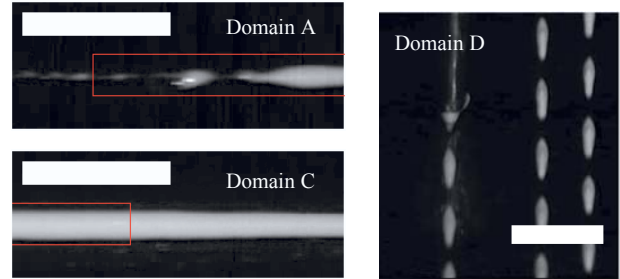


Fig. 8. Deposition images from the nominal pulse-type input response. Bounding boxes show rod shape for perfect reference tracking. All scale bars are 2 mm.

#### IV. ILC IMPLEMENTATION

The typical ILC flow diagram is modified when the output signal is measured post-process. Instead of the output signal directly feeding into memory, an arbitrarily long processing time delay,  $q^{-Proc}$ , is added to the system, Figure 9. The processing delay does not change the dynamics because all operations are suspended between iterations.

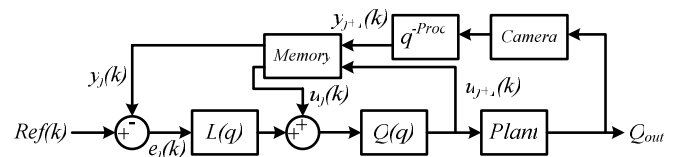


Fig. 9. Vision based ILC for  $\mu$ RD flow diagram.

Two different learning functions were tested. The first was a P-type learning function with the form:

$$u_{j+1}(k) = u_j(k) + k_p e_j(k+1) \quad (13)$$

The second learning controller was a model inversion learning function with the form:

$$u_{j+1}(k) = u_j(k) + k_p \hat{P}^{-1}(q) e_j(k) \quad (14)$$

The inverse plant,  $\hat{P}^{-1}(q)$ , was a modified discrete time version of the inverse of (11). A fast zero was added to the plant model in order to make the inversion proper. First order system parameters were empirically determined based on the falling step response, Domain C, of the nominal plant in Figure 7 of Section III.  $\hat{P}^{-1}(q)$  had the frequency response seen in Figure 10, where there is a deviation between the continuous time and discrete time system at frequencies above 100 rad/s because of the fast zero added to make the inversion proper.

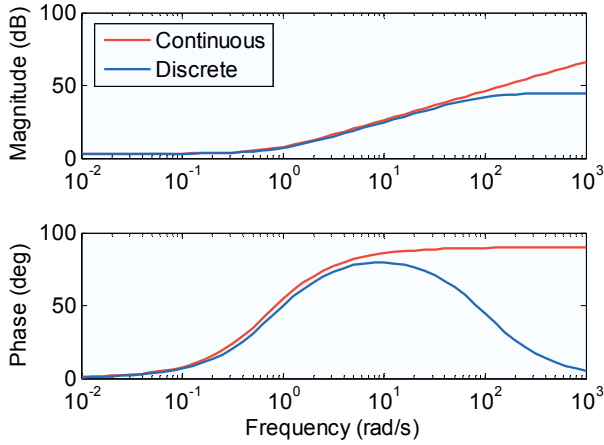


Fig. 10. Frequency response of  $\hat{P}^{-1}(s)$  and  $\hat{P}^{-1}(q)$ . The continuous and discrete time systems deviate at frequencies above 100 rad/s.

For both (13) and (14) the next iteration control signal was filtered using a second order Butterworth filter, with the filtering operation applied both forwards and backwards for zero phase shift. Learning controller gain,  $k_p$ , and Q-filter bandwidth were chosen to be the constants presented in Table II.

TABLE II  
LEARNING FUNCTION PARAMETERS

Controller Type	$k_p$	Bandwidth (Hz)
P-type	0.40	15
Model Inversion	0.25	6

## V. RESULTS

### A. P-type ILC

Results from the P-type learning function, (13), are shown in Figure 11. After a sufficient number of iterations, P-type learning control significantly improves the reference tracking of the micro-extrusion system. The time delay and slow rise time seen in the nominal response in Domain A is improved as is the steady-state tracking, Domain B. Additionally, the long decay time in Domain C and intermittent flow behavior

in Domain D seen without ILC is minimal by comparison. Although the response is improved over the nominal response, the system exhibits a large overshoot that grows with each subsequent iteration.

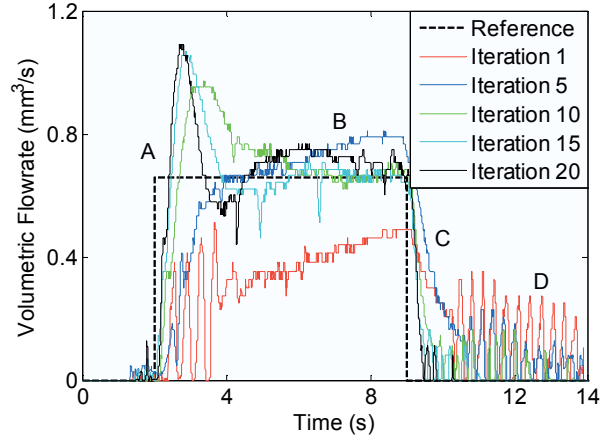


Fig. 11. P-type ILC response to the pulse-type input. Response is divided into 4 domains, (A) rising step response, (B) steady-state response, (C) falling step response, (D) and intermittent flow behavior domain.

### B. Model Inversion ILC

The model inversion ILC, (14), provides better reference tracking results, as seen in Figure 12. There is a minimal overshoot at the rising step, Domain A. Also the measured flowrate tracks the reference flowrate at steady-state, Domain B, and the intermittent flow behavior in Domain D decreases with each iteration.

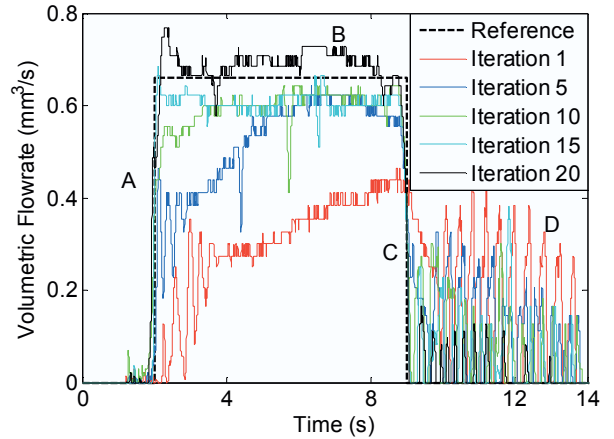


Fig. 12. Model inversion ILC response to the pulse-type input. Response is divided into 4 domains, (A) rising step response, (B) steady-state response, (C) falling step response, (D) and intermittent flow behavior domain.

### C. Comparison of P-type and model inversion ILC

The superiority of model inversion ILC over P-type ILC is evident when comparing RMS errors, Figure 13. The model inversion controller converges to a lower RMS primarily because the system does not overshoot the reference trajectory like the P-type controller. Also, the system has a

faster rise and decay time in Domains A and C, respectively, and tracks better in steady-state, Domain B. After 20 iterations, the model inversion controller decreases RMS error to less than 20% of the original value at iteration 1, as compared to less than 45% for the P-type controller.

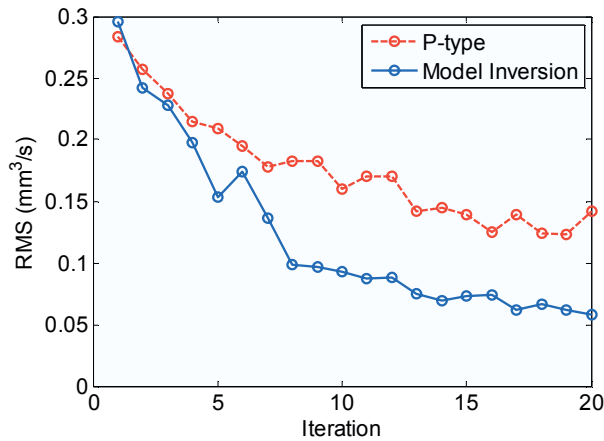


Fig. 13. RMS error at each iteration for the P-type and model inversion ILC.

Furthermore, the benefits of the model inversion are evident in the images of the 20th iteration, Figure 14. The large overshoot in the volumetric flowrate is clearly shown in the right side of the P-type controller image of Domain A; whereas the rods of ink deposited with the model inversion controller closely approximate the ideal rod shape.

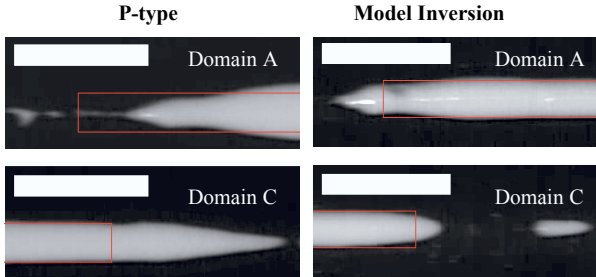


Fig. 14. Deposition images of iteration 20 using P-type and model inversion ILC. Bounding boxes show rod shape for perfect reference tracking. All scale bars are 2 mm.

The model inversion controller more accurately tracks the reference signal because model (11) developed in Section III is accurate. When (11) is inverted for the model inversion ILC, the resultant learning function is a high pass filter, Figure 10. Inherent to this high pass filter is a derivative term that enables the control signal to react more quickly than the P-type controller to the rising and falling steps and the overshoot seen in Figure 11. As seen in Figure 15, the model inversion control signal rises and decays more rapidly than the P-type control signal, promoting better tracking of the pulse-type input. The consequences of a higher frequency content control signal are not all beneficial. In Domain D, the high frequency output signal from the intermittent flow behavior is amplified by the high pass filter, causing the control signal to oscillate around zero

where the ideal signal would asymptotically approach zero, Figure 15. Qualitatively, the P-type controller retracts the extrusion system plunger at the falling step, pulling a vacuum on the ink reservoir to quickly terminate ink flow. However, the model inversion controller quickly retracts the plunger then pushes forward again as a result of the high amplitude response to abrupt changes in measured flowrate. Consequently, the model inversion controller does not eliminate the intermittent flow behavior in Domain D as well as the P-type controller.

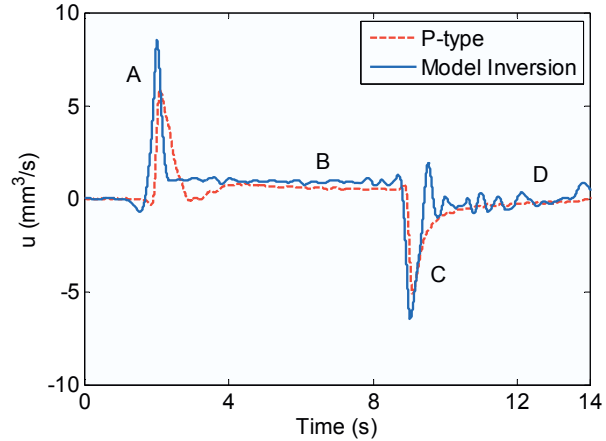


Fig. 15. Control signal calculated by the P-type and model inversion ILC for iteration 21.

## VI. EXAMPLE EXPERIMENT

Visual results of two closed test shapes, a triangle and a circle, are shown in Figure 16. Ink extrusion using the nominal reference signal as the control signal performs poorly, leaving the perimeter of both shapes open and extruding a length of ink beyond the perimeter of the shapes. The model inversion ILC significantly improves the extrusion performance, both seamlessly closing the perimeter of the shapes and minimizing the amount of excess ink outside the perimeter.

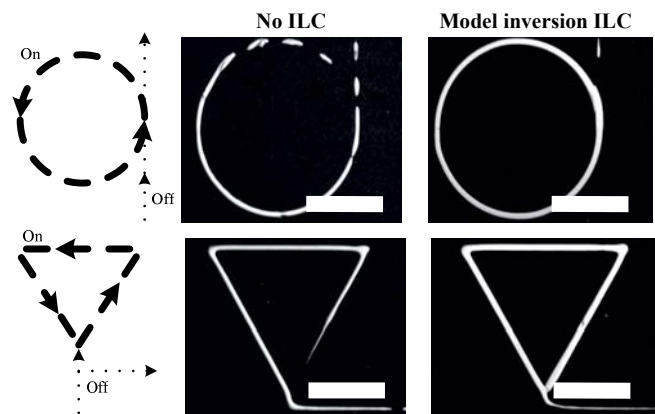


Fig. 16. Deposition of two tests shapes. The cartoons on the left display the intended trajectory. Ink extrusion is turned ‘Off’ during the dotted line segment and ‘On’ during the dashed line segment. In both cases, the shapes deposited without ILC deposit incorrectly and the shapes with model inversion ILC are much improved. Scale bars are 5 mm.

## VII. CONCLUSIONS

Currently,  $\mu$ RD uses a steady-state ink flowrate, inhibiting the fabrication of structures with complex architectures. The results here show the ability to use machine vision incorporated into an ILC framework to precisely modulate ink flowrate, enabling the deposition of complex architectures. The vision system accurately measures the volumetric flowrate for this specific application, but similar vision systems have potential uses in other ILC applications. To implement a model inversion ILC, a model of the nominal plant was developed. The nominal system model has a first order response with a long time delay, slow time constant, and a steady-state offset. These poor dynamic properties are improved by both P-type and model inversion ILC algorithms. The P-type learning controller significantly decreases rise and decay times to a pulse-type input and decreases the steady-state offset, however the system overshoots the reference trajectory. The model inversion learning controller improves on the P-type controller, accurately tracking the reference with minimal overshoot and therefore converging to a lower RMS error. The improvement is a result of the inherent derivative from the model inversion, however there is a consequence to the derivative term. The derivative causes the system to react to sharp changes in the measured flowrate during a period of intermittent ink flow, causing the control signal to oscillate. When comparing the two controllers using the Domains given in Figure 7, the model inversion ILC performs better in Domains A, B, and C whereas the P-type ILC performs better in Domain D. This suggests that future work may include time varying algorithms. Finally, an example relevant to the deposition of interstitial structures, such as embedded micro-sized sensors, displays that the model inversion ILC properly extrudes the ink, producing structures with a seamless perimeter and minimal excess material outside the perimeter.

## ACKNOWLEDGMENT

The authors would like to acknowledge Dr. Doug Bristow for his help with the ILC implementation and tuning.

## REFERENCES

- 1 Bristow, D.A., Tharayil, M., and Alleyne, A.G., "A Survey of Iterative Learning Control," *IEEE Control Systems Magazine*, pp. 96-114, 2006.
- 2 Lee, K.S. and Lee, J.H., "Iterative Learning Control-Based Batch Process Control Technique for Integrated Control of End Product Properties and Transient Profiles of Process Variables," *Journal of Process Control*, vol. 13, pp. 607-621, 2003.
- 3 Cesarano, J., Segalman, R., and Calvert, P., "Robocasting Provides Moldless Fabrication From Slurry Deposition," *Ceramic Industry*, vol. 148, no. 4, pp. 94-102, 1998.
- 4 Smay, J.E., Cesarano III, J., and Lewis, J.A., "Colloidal Inks for Directed Assembly of 3-D Periodic Structures," *Langmuir*, vol. 18, no. 14, pp. 5429-5437, 2002.
- 5 Michna, S., Wu, W., and Lewis, J.A., "Concentrated Hydroxyapatite Inks for Direct-Write Assembly of 3-D Periodic Scaffolds," *Biomaterials*, vol. 26, pp. 5632-5639, 2005.
- 6 Miranda, P., Saiz, E., Gryn, K., and Tomsia, A.P., "Sintering and Robocasting of  $\beta$ -Tricalcium Phosphate Scaffolds for Orthopaedic Applications," *Acta Biomaterialia*, vol. 2, pp. 457-466, 2006.
- 7 Smay, J.E., Cesarano III, J., Tuttle, B.A., and Lewis, J.A., "Piezoelectric Properties of 3-X Periodic  $\text{Pb}(\text{Zr}_x\text{Ti}_{1-x})\text{O}_3$ -Polymer Composites," *Journal of Applied Physics*, vol. 92, no. 10, pp. 6119-6127, 2002.
- 8 Therriault, D., White, S.R., and Lewis, J.A., "Chaotic Mixing in Three-Dimensional Microvascular Networks Fabricated by Direct-Write Assembly," *Nature Materials*, vol. 2, pp. 265-271, 2003.
- 9 Gratson, G.M., Xu, M., and Lewis, J.A., "Direct Writing of Three-Dimensional Webs," *Nature*, vol. 428, pp. 386, 2004.
- 10 Hoelzle, D.J., "Reliability Guidelines and Flowrate Modulation for a Micro Robotic Deposition System," M.S. Thesis, Department of Mechanical Science and Engineering, University of Illinois at Urbana-Champaign, Urbana, IL, 2007.
- 11 Han, W. and Jafari, M.A., "Coordination Control of Positioning and Deposition in Layered Manufacturing," *IEEE Transactions on Industrial Electronics*, vol. 54, no. 1, pp. 651-659, 2007.
- 12 Bristow, D. and Alleyne, A., "A Manufacturing System for Microscale Robotic Deposition," *Proceedings of the American Controls Conference*, pp. 2620-2625, 2003.
- 13 Bellini, A., Güçeri, S., and Bertoldi, M., "Liquefier Dynamics in Fused Deposition," *Journal of Manufacturing Science and Engineering*, vol. 126, pp. 237-246, 2004.
- 14 Chhabra, R.P., Richardson, J.F., *Non-Newtonian Flow in the Process Industries*. Oxford, UK: Butterworth-Heinemann, 1999.